BBA - Molecular Cell Research 1870 (2023) 119367

Contents lists available at ScienceDirect

BBA - Molecular Cell Research

journal homepage: www.elsevier.com/locate/bbamcr

Research paper

Synchrotron Fourier-Transform Infrared Microspectroscopy: Characterization of *in vitro* polarized tumor-associated macrophages stimulated by the secretome of inflammatory and non-inflammatory breast cancer cells

Hossam Taha Mohamed [a,b,*], Gihan Kamel [c,d], Noura El-Husseiny [a], Aya Ali El-Sharkawy [a], Ahmed A. El-Sherif [e], Mohamed El-Shinawi [f,g], Mona Mostafa Mohamed [a,h]

[a] Zoology Department, Faculty of Science, Cairo University, Giza 12613, Egypt
[b] Faculty of Biotechnology, October University for Modern Sciences and Arts, Giza 12451, Egypt
[c] Synchrotron-light for Experimental Science and Applications in the Middle East (SESAME), Allan, Jordan
[d] Department of Physics, Faculty of Science, Helwan University, Cairo 11795, Egypt
[e] Chemistry Department, Faculty of Science, Cairo University, Giza 12613, Egypt
[f] Department of General Surgery, Faculty of Medicine, Ain Shams University, Cairo, 11566, Egypt
[g] Faculty of Medicine, Galala University, Suez 43511, Egypt
[h] Faculty of Science, Galala University, Suez 43511, Egypt

ARTICLE INFO

Keywords:
Inflammatory breast cancer
Tumor-associated macrophages
Synchrotron FTIR microspectroscopy
Tumor-infiltrating monocytes

ABSTRACT

Studies suggested that the pathogenesis of inflammatory breast cancer (IBC) is related to inflammatory manifestations accompanied by specific cellular and molecular mechanisms in the IBC tumor microenvironment (TME). IBC is characterized by significantly higher infiltration of tumor-associated macrophages (TAMs) that contribute to its metastatic process *via* secreting many cytokines such as TNF, IL-6, IL-8, and IL-10 that enhance invasion and angiogenesis. Thus, there is a need to first understand how IBC-TME modulates the polarization of TAMs to better understand the role of TAMs in IBC. Herein, we used gene expression signature and Synchrotron Fourier-Transform Infrared Microspectroscopy (SR-μFTIR) to study the molecular and biochemical changes, respectively of *in vitro* polarized TAMs stimulated by the secretome of IBC and non-IBC cells. The gene expression signature showed significant differences in the macrophage's polarization-related genes between stimulated TAMs. FTIR spectra showed absorption bands in the region of 1700–1500 cm^{-1} attributed to the amide I ν(C=O), & ν_{AS} (C—N), δ (N—H), and amide II ν(C—N), δ (N—H) proteins bands. Moreover, three peaks of different intensities and areas were detected in the lipid region of the νCH_2 and νCH_3 stretching modes positioned within the 3000–2800 cm^{-1} range. The PCA analysis for the second derivative spectra of the amide regions discriminates between stimulated IBC and non-IBC TAMs. This study showed that IBC and non-IBC TMEs differentially modulate the polarization of TAMs and SR-μFTIR can determine these biochemical changes which will help to better understand the potential role of TAMs in IBC.

1. Introduction

Breast cancer is the most common type of cancer among women in the middle east and its incidence has substantially increased in recent years, especially among women younger than fifty [1]. Many breast cancer patients do not die due to their primary tumor but from metastasis [2]. Inflammatory breast cancer (IBC) is the most aggressive and metastatic phenotype of breast cancer [3]. The prevalence of IBC is quite low but it is characterized by rapid progression and poor prognosis [4]. The treatment strategy of IBC is built on the combination of Chemotherapy, Surgery, radiotherapy, and targeted therapy because of the lack of specific therapy [5]. Previous studies suggested that the pathogenesis of IBC is related to inflammation due to inflammatory manifestations and changes in the tumor microenvironment (TME) [3,4].

* Corresponding author at: Faculty of Biotechnology, October University for Modern Sciences and Arts, Giza 12451, Egypt.
E-mail address: hotaha@msa.edu.eg (H.T. Mohamed).

https://doi.org/10.1016/j.bbamcr.2022.119367
Received 22 June 2022; Received in revised form 13 September 2022; Accepted 26 September 2022
Available online 3 October 2022

TME is composed of cancer cells, non-cancerous stromal cells, blood vessels, and extracellular matrix molecules with a complicated cell signaling network [6,7]. Stromal cells mainly include tumor-associated macrophages (TAMs), endothelial cells, and cancer-associated fibroblasts (CAFs). TAMs are the most incident stromal cells and play a potential role in cancer progression [7]. Cancer cells secrete many chemokines to attract monocytes to infiltrate cancer tissues and promote their polarization. TAMs originated from the polarization of $Ly6C^{+}CCR2^{+}$ circulating monocytes, which are derived from hematopoietic stem cells in the bone marrow [8]. Moreover, tissue-resident macrophages also differentiated to TAMs [9]. Initially, monocytes are polarized into 2 major phenotypes of macrophages: pro-inflammatory M1 phenotype, and anti-inflammatory M2 phenotype [10]. The polarization and phenotype switching of macrophages is accompanied by dramatic changes in cell transcriptome and proteome that are regulated by exogenous and intrinsic stimuli [11]. M1 macrophages secrete cytokines and chemokines involved in the activation and attraction of lymphocytes to the inflammation site. In addition, M1 macrophages perform antigen-presentation to induce the humoral immune response [12]. M1 macrophages generate nitric oxide (NO) from arginine to damage and kill pathogens *via* the formation of peroxynitrite. In addition, M1 macrophages suppress cell proliferation and promote tissue damage. In contrast, M2 macrophages control inflammatory response *via* secreting anti-inflammatory cytokines and participate in wound healing, post-inflammatory tissue repair, and remodeling [12]. Moreover, M2 macrophages induce cells to proliferate and tissue regeneration [11]. M2 macrophages expressing anti-inflammatory cytokine lead to increased tumor growth, invasion, and metastasis [3]. In contrast to the original role of macrophages in phagocytosis, M2-like TAMs promote cancer cell migration and invasion and neutralize the cytotoxicity activity of $CD8^{+}$ T cells to promote cancer progression [7].

IBC is characterized by significantly higher infiltration of TAMs [3]. In IBC, TAMs produce high levels of inflammatory cytokines that promote the survival and proliferation of IBC cells [13]. In addition, TAMs contribute to the metastatic process in IBC patients *via* secreting many cytokines such as TNF, IL-6, IL-8, and IL-10 that enhance invasion and angiogenesis [14]. It was demonstrated that tumor-infiltrating monocytes isolated from IBC patients significantly expressed these cytokines higher than those from non-IBC patients [3].

Because of these findings, there is increasing interest in studying the role of TAMs in IBC progression to be a potential therapeutic target. To understand this role there is a need to first determine how IBC TME affects the polarization of tumor-infiltrated monocytes into mature TAMs *via* using a sensitive and accurate analytical tool to give full information about any biochemical changes independently of morphological changes and cell surface markers. Among the numerous analytical tools in the cancer field, Fourier transform Infrared microspectroscopy is a highly advanced analytical approach used in the diagnosis of many diseases including cancer as it can detect any biochemical changes even before any morphological changes and translate these biochemical changes into a characteristic spectral signature that corresponds with the irradiated infrared light [15,16]. Recently, Mohamed and colleagues used FTIR microspectroscopy in the characterization of IBC at the cellular and tissue level [17]. Moreover, they differentiated between non-IBC and IBC cells depending on their Glycosaminoglycans (GAGs) synthesis capacity using synchrotron-FTIR microspectroscopy (SR-μFTIR) and imaging [18]. Kumar and colleagues used FTIR microspectroscopy and imaging with multivariate statistical analyses in the characterization of fibroblasts stimulated by various breast cancer cell lines [19]. The obtained results showed that FTIR microspectroscopy and imaging easily differentiate between stimulated and unstimulated fibroblasts, but not between fibroblasts stimulated by different breast cancer cell lines [19]. Depending on these previous studies, herein we used gene expression signature and SR-μFTIR to study the gene expression and biochemical changes of *in vitro* polarized TAMs stimulated by the secretome of IBC and non-IBC cells.

2. Materials and methods

2.1. Patient samples

This study was approved by the Institutional Review Board (IRB#00006379), Faculty of Medicine, Ain Shams University, Egypt. A total of 40 breast cancer patients (20 non-IBC and 20 IBC) were enrolled in the present study. IBC and Non-IBC patients were clinically and pathologically diagnosed as previously described [3,20,21]. Patients suffering from Hepatitis or AIDS or COVID-19 or auto-immune diseases were excluded from this study. Before participation, all patients signed consent forms, including approval for publication of the study results.

2.2. Immunohistochemistry

Immunohistochemical (IHC) staining was performed after chemical dewaxing of 4 μm thick formalin-fixed paraffin-embedded (FFPE) tissue sections as described before [20,22] using antibodies for MAC387 (1 μg/mL) (Abcam, Cambridge, UK). The stained area fractions were calculated using ImageJ software (National Institutes of Health, Bethesda, MD, USA) [21,23].

2.3. Isolation of tumor-infiltrating monocytes

During axillary dissection in MRM operations, 10 mL of blood was withdrawn from the identified axillary tributaries in a heparinized syringe with an angular needle as described before [24]. Plasma was collected from the whole blood sample *via* centrifugation at 1500 rpm for 30 min. Mononuclear cells were separated from the precipitated blood content by Ficoll-Hypaque density gradient centrifugation (Lonza, ME, USA) at 1500 rpm for 30 min. The buffy coat layer containing mononuclear cells was separated and washed twice with PBS. The $CD14^{+}$ monocytes were purified from the mononuclear cells using the "EasySep™ Human Monocyte Enrichment Kit without CD16 Depletion" (StemCell Technologies, Vancouver, Canada). Purified tumor-infiltrating $CD14^{+}$ monocytes were seeded overnight at a concentration of (1×10^{6} cells/mL) in RPMI media with 1 % of penicillin/streptomycin antibiotic mixture in 3 % fetal bovine serum (FBS) and incubated at 37 °C in 5 % CO_2 for 24 h. The isolated tumor-infiltrating monocytes were aliquoted and stored in growth media with 10 % DMSO in liquid nitrogen till use.

2.4. Immunophenotype of mononuclear cells isolated from IBC and non-IBC TME blood

The mononuclear cells were suspended in 100 μL staining buffer (PBS, 1 % BSA) and 5 μL of the following fluorochrome-labeled monoclonal antibodies: CD14-FITC, CD16-PECye5, and HLA-DR-PE (eBioscience San Diego, CA, USA) were added and incubated in dark for 30 min. Cells were washed twice with PBS to discard unbound antibodies and 50,000 events were acquired on CyFlow Cube 8 flow cytometry (Sysmex Partec, Muenster, Germany). Data analysis was performed using FCS EXPRESS 4 cytometry software (BD Biosciences, CA, USA) and results were expressed as mean ± SD.

2.5. Breast cancer cell lines

Human breast cancer cell lines MCF7 (ATCC® HTB-22™) and MDA-MB-231 (ATCC® HTB-26™) were obtained from the American Type Cell Collection (ATCC, VA, USA), and SUM149 breast cancer cell line was a gift from Prof. Robert J. Schneider (Department of Microbiology, New York University School of Medicine, NYC, USA) were used in this study. MCF7 and MDA-MB-231 cells were cultured in RPMI and DMEM media, respectively with 10 % FBS and 1 % of penicillin/streptomycin antibiotic mixture. SUM149 cells were cultured in HAM's F12 medium with 5 % FBS, 5 mM HEPES, 1 μg/mL Hydrocortisone, 5 μg/mL insulin, and 1

% of penicillin/streptomycin antibiotic mixture. All cell lines were incubated in a humidified incubator at 37 °C in 5 % CO_2. Cells secretome was collected after 24 h starvation and concentrated at 1:100 using Vivaspin™ protein concentrator column (Sartorius, Goettingen, Germany) with 10,000 molecular weight cutoff value (MWCO value). The protein content of each type of cell secretome was determined *via* Bradford assay (Biorad Laboratories, CA, USA) using a Multiskan sky microplate spectrophotometer (Thermo Scientific, MA, USA).

2.6. In vitro polarization of tumor-infiltrated monocytes by the secretome of different breast cancer cells

Tumor-infiltrating monocytes (3×10^5 cell/well) were seeded in growth media conditioned with (2000 ng/mL) of the secretome of MCF7, MDA-MB-231, and SUM149 cells and incubated for 8 days in a humidified atmosphere at 37 °C in 5 % CO_2. It should be noted that media were renewed every two days. Cells were aliquoted and stored at −80 °C for RNA extraction. Secretome of *in vitro* polarized TAMs was collected and concentrated 1:100 using Vivaspin™ protein concentrator column (Sartorius, Goettingen, Germany) with 10,000 molecular weight cutoff value (MWCO value) and its protein content was determined *via* Bradford assay (Biorad Laboratories, CA, USA) using Multiskan sky microplate spectrophotometer (Thermo Scientific, MA, USA). Cells were aliquoted and stored at −80 °C for RNA extraction.

2.7. Microscopic examination of in vitro polarized TAMs

For cellular morphology of *in vitro* polarized TAMs, microscopic images were taken at 40× magnification. Three distinct morphologic subtypes were identified, M0 were small/roundish cells characterized by a cellular diameter ≤ 10 μm with the absence of cytoplasmic projections on the cell surface, M1 were enlarged amoeboid cells characterized by a cellular diameter ≥ 10 μm and presence of many delicate cytoplasmic extensions on the cell surface with visible intracellular vacuoles, and M2 demonstrated a large and elongated "spindeloid" cells with a cellular diameter between 10 and 30 μm and cytoplasmic extensions on the apical ends of the cell bodies [25,26].

2.8. Gene expression signature analysis of in vitro polarized TAMs

To confirm the effect of the secretome of IBC and non-IBC cells on the polarization status of *in vitro* polarized TAMs, based on previous studies [27–34], we carefully designed and customized PCR array that included 43 macrophages polarization-related genes (Vivantis, Selangor, Malaysia) to analyze the gene expression signature of *in vitro* polarized TAMs. Total RNA was extracted from stimulated tumor infiltrated monocytes using GeneJET™ RNA purification Kit (Thermo Fisher Scientific, MA, USA). The total RNA concentration was measured by a Multiskan SkyHigh microplate spectrophotometer (ThermoFisher Scientific, MA, USA), and RNA integrity was tested by separating the RNA on a 1 % standard agarose gel and examining the ribosomal RNA bands. The RNA extracts showing a 260/280 nm ratio between 1.8 and 2.1 were selected for cDNA transcription. One μg of total RNA was reverse transcribed into complementary DNA using RevertAid First Strand cDNA Synthesis Kit (Thermo Fisher Scientific, MA, USA). The quantitative real-time PCR was conducted using SYBR Green dye (Thermo Fisher Scientific, MA, USA) and gene expression levels were measured in an AriaMX real-time PCR System (Agilent, CA, USA). PCR amplification specificity was verified using melting curve analysis. All samples were run in triplicate, and normalized to the CTs of *18S*, *ACTB*, *B2M*, *GAPDH*, and *HPRT* housekeeping genes and analyzed using Pfaffl's method [35].

2.9. Enrichment analysis of differentially expressed genes

GeneMANIA (http://genemania.org/) was used to compare the correlation between DEGs obtained from gene expression signature analysis of different *in vitro* polarized TAMs stimulated by the secretome of IBC and non-IBC cells and neighboring related genes. In addition, Metascape (http://metascape.org/gp/index.html#/main/step1) is a public online analysis database that was used for functional annotation and enrichment analysis based on Gene Ontology (GO), Kyoto Encyclopedia of Genes and Genomes (KEGG), Reactome, canonical pathways, and hallmark gene terms. The analysis was based on the relevant parameters as follows: minimum overlap, 3; *P*-value cutoff, 0.01 and minimum enrichment 1.5. All protein-protein interactions among input genes were extracted from the PPI data source and formed a PPI network. GO enrichment analysis was applied to the network to extract "biological meanings". The MCODE algorithm was then applied to this network to identify neighborhoods where proteins are densely connected [36–39].

2.10. SR-μFTIR fixed single-cell analysis

To understand the biochemical changes that occurred inside *in vitro* polarized TAMs after stimulation by the secretome of IBC and non-IBC cells, we targeted the cytoplasms of the polarized TAMs using the SR-μFTIR technique at the BM02-IR beamline [40,41] in SESAME (Synchrotron-light for Experimental Science and Applications in the Middle East) light source, Jordan. Tumor-infiltrating monocytes were seeded on CaF_2 substrate and seeded in growth media conditioned by the secretome of IBC and non-IBC cells as described above. The *in vitro* polarized TAMs on CaF_2 substrates were washed three times with PBS and then fixed with 4 % paraformaldehyde (PFA) for 20 min and washed three times with sterile distilled water, then left to air-dry. Cells were analyzed with SR-μFTIR as we described before [18]. The IR beam is directed to an endstation of a Nicolet Continuum IR microscope equipped with an MCT (Mercury Cadmium Telluride) single-element detector and coupled to the 8700 Thermo FTIR Spectrometer (ThermoFisher Scientific, MA, USA). Samples were placed on the Prior© scan motorized stage. OMNIC© v. 9.2.41 software package (Thermo Fisher Scientific, USA) was used for the data collection. The endstation is purged with dry air to reduce the spectral influence of water vapor and carbon dioxide. IR data were collected through a double path single masking aperture size of $10x10\mu m^2$ and a pair 32× Schwarzschild objective and condenser. 512 co-added scans of background spectra were collected to assess their contribution. Measurements were conducted in transmission mode with a diamond compression cell in the Mid-IR (4000–650 cm^{-1}) range with a spectral resolution of 4 cm^{-1} and 256 co-added scans, levels Zero filling 1, and Happ-Genzel apodization window.

2.11. Spectral data analysis

FTIR spectral pre-processing was applied to the collected raw spectra using OMNIC© software. The raw spectra displaying noise or significant absorptions due to water vapor and CO2 were excluded. The remaining spectra were baseline corrected and smoothed with 9 points and 2nd polynomial order using Gaussian smoothing. Curve fitting and Savitzky-Golay's second derivatives were performed by PeakFit© V4.12 software (Copyright©2020 Systat Software, Inc.).

2.12. Multivariate Statistical Analysis

The multivariate statistical analysis was performed with The Unscrambler© X v.10.4 software (CAMO Analytics, Oslo, Norway) employing Principal Component Analysis (PCA). The analysis was applied to the two mainly involved spectral regions; the protein region (1700–1500 cm^{-1}), and the lipid region (3050–2800 cm^{-1}). Second derivatives were calculated and smoothed with 7 smoothing points and 3rd polynomial order using Savitzky-Golay's algorithm, followed by range normalization.

2.13. Statistical analysis

The Statistical Package of the Social Sciences software (SPSS, Chicago, IL, USA), version 22.0 was used for data analysis. The data were presented as the mean ± standard deviation (SD). In addition, differences among two groups of variables were evaluated using Student's *t*-test, Wilcoxon test, and Chi-square test. The statistical difference between more than two groups was evaluated using one-way ANOVA followed by Tukey's HSD *Post Hoc* tests. The level of significance was set at $P < 0.05$.

3. Results

3.1. Clinical and pathological characterization of non-IBC and IBC patients

According to the American Joint Committee on Cancer (AJCC), IBC is an aggressive locally advanced breast cancer phenotype and is classified as T4d [42,43]. The incidence of dermal tumor emboli is one of the pathological characteristics of IBC. The number and size of emboli in IBC patients are significantly numerous and larger compared to non-IBC patients [6]. Herein the statistical analysis showed that there were no significant differences in patient ages, pathological type, tumor grades, ER, PR, and HER-2 between IBC and non-IBC patients. On the other hand, IBC patients were characterized by significantly larger tumor size, high numbers of metastatic lymph nodes, and high incidence of lymphovascular invasion with the presence of dermal tumor emboli (Fig. 1A) ($P = 0.004$, 0.049, 0.001, and 0.0001, respectively) compared to non-IBC patients as described in Table 1.

3.2. IBC cancer tissues are characterized by significant high infiltration of MAC387$^+$ TAMs

It was demonstrated that a high incidence of migratory TAMs correlated with aggressiveness and worse outcomes in breast cancer [44]. Herein, we determined the infiltration of MAC387$^+$ TAMs in IBC and non-IBC cancer tissues. Statistical analysis showed significantly high infiltration of MAC387$^+$ TAMs in IBC cancer tissues ($P = 0.04$) compared to non-IBC cancer tissues (Fig. 1B and C).

3.3. Immunophenotyping analysis of mononuclear cells isolated from TME

The flow cytometry analysis of mononuclear cells isolated from TME revealed a nonsignificant high percentage of CD14$^+$, CD16$^+$, and HLA-DR$^+$ cell surface markers in the TME blood collected from IBC ($n = 20$) compared to non-IBC (n = 20) patients (Fig. 1D and E).

3.4. Microscopic examination and gene expression signature of in vitro polarized TAMs

The microscopic examination showed that the secretome of MCF7, MDA-MB-231, and SUM149 cells polarized tumor-infiltrating monocytes towards M1/M2 TAMs (Fig. 2A). The gene expression signature analysis showed that the secretome of MCF7, MDA-MB-231, and SUM149 cells activates the polarization of tumor-infiltrating monocytes

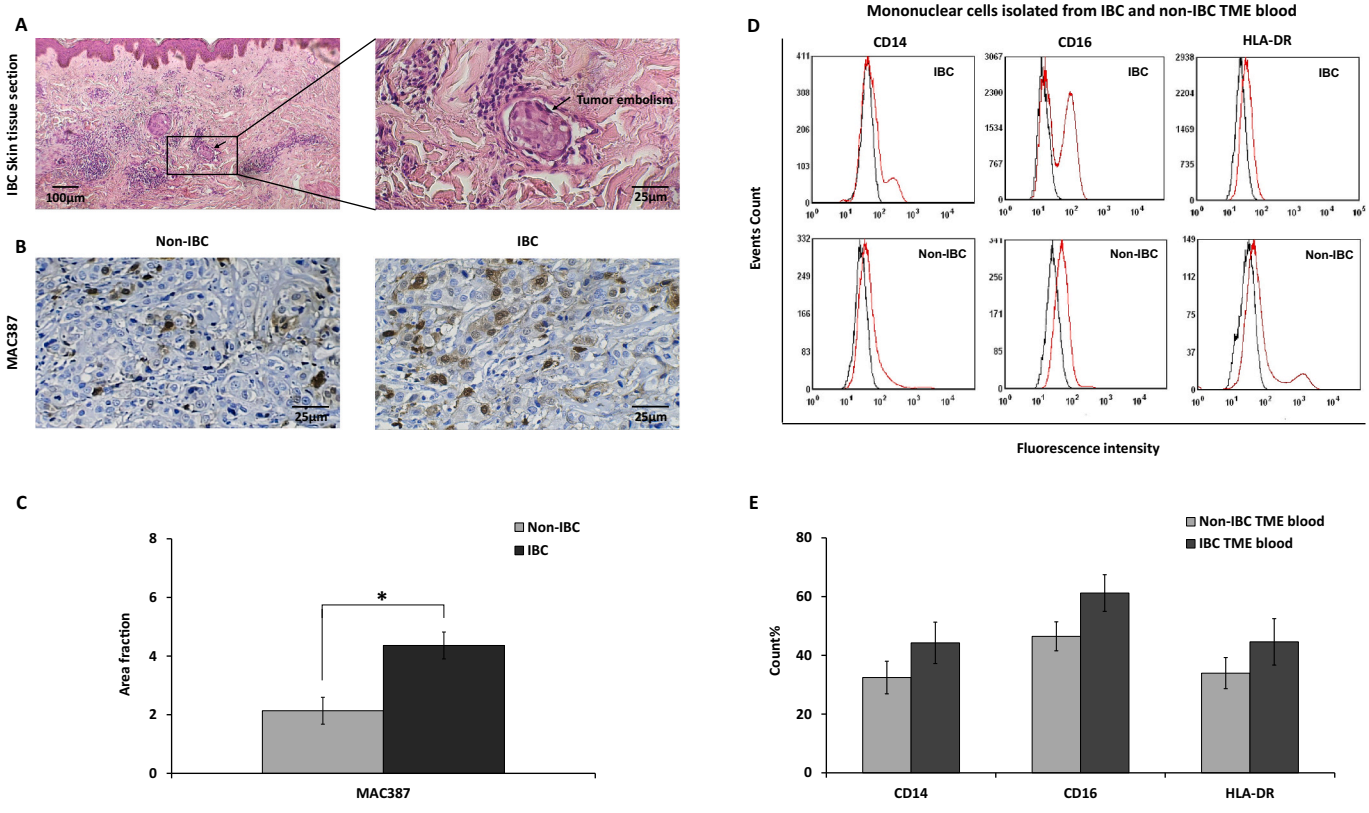

Fig. 1. Immunohistochemical staining of MAC387$^+$ TAMs in IBC and non-IBC cancer tissues and immunophenotyping of mononuclear cells isolated from IBC and non-IBC TME blood. (A) Microscopic images of H and E stained paraffin embedded skin tissue sections of IBC showed the incidence of tumor embolism (Magnification scale for the left image was 10× and for the right image 40×). (B) Microscopic images of MAC387 stained paraffin-embedded IBC cancer tissue sections (Magnification scale 40×) (C) bars showed a significantly high prevalence of MAC387$^+$ TAMs among IBC cancer tissue compared to non- IBC cancer tissues. Data represented the mean of ±SD. *P* values were calculated using the Student *t*-test, where * represented ($P < 0.05$). (D) Representative histograms for cell staining for CD14-FITC, CD16-PECye5, and HLA-DR-PE for IBC and non-IBC mononuclear cells isolated from TME blood. (E) Cumulative data for the mean percentage for all stained markers. Data represented the mean of ±SD. *P* values were calculated using the Wilcoxon test, where * represented ($P < 0.05$).

Table 1
Clinical and pathological characterization of IBC *versus* non-IBC patients.

Characteristic	Non-IBC (n = 20)	IBC (n = 20)	P-value
Age [year]			
Range	31–67	29–75	0.094[a]
Mean ± SD	50.1 ± 9.55	44.2 ± 12.1	
Tumor size [cm]			
Mean ± SD	4.34 ± 2.2	6.7 ± 2.65	0.004**,[a]
Pathological type			
Invasive ductal carcinoma	19 (95 %)	15 (75 %)	0.091[b]
Invasive lobular carcinoma	1 (5 %)	5 (25 %)	
Tumor grade			
G1	1 (5 %)	0 (0 %)	0.468[b]
G2	15 (75 %)	13 (65 %)	
G3	4 (20 %)	6 (30 %)	
G4	0 (0 %)	1 (5 %)	
Number of metastatic axillary lymph nodes			
Mean ± SD	5 ± 6.1	9.6 ± 6.6	0.049*,[a]
Lymphovascular invasion			
Negative	17 (85 %)	6 (30 %)	0.001**,[b]
Positive	3 (15 %)	14 (70 %)	
Dermal tumor emboli			
Negative	19 (95 %)	0 (0 %)	0.0001**,[b]
Positive	1 (5 %)	20 (100 %)	
ER			
Negative	11 (55 %)	16 (80 %)	0.088[b]
Positive	9 (45 %)	4 (20 %)	
PR			
Negative	12 (60 %)	15 (75 %)	0.251[b]
Positive	8 (40 %)	5 (25 %)	
HER-2			
Negative	12 (60 %)	13 (65 %)	0.514[b]
Positive	8 (40 %)	7 (35 %)	

Data are reported as means ± SD.
[a] Student's *t*-test.
[b] Chi-square test.
* Significant P value ($P < 0.05$).
** Significant P value ($P < 0.01$).

towards M1/M2 TAMs. The statistical analysis showed significant variations in the mRNA expression of the macrophage polarization-related genes between *in vitro* polarized TAMs stimulated by the secretome of MCF7, MDA-MB-231, and SUM149 cells (Fig. 2B). The mRNA level of *IL-10* and *TLR1* were significantly ($P < 0.05$) high expressed in the *in vitro* polarized TAMs stimulated by the secretome of SUM149 cells compared to MCF7 and MDA-MB-231 cells. The mRNA level of *TNF* was significantly ($P < 0.05$) high expressed in the *in vitro* polarized TAMs stimulated by the secretome of MCF7 cells compared to MDA-MB-231 and SUM149 cells. Moreover, the mRNA level of *CD68* and *ARG1* were significantly ($P < 0.05$) high expressed in the *in vitro* polarized TAMs stimulated by the secretome of MDA-MB-231 and SUM149 cells compared to MCF7 cells, while the mRNA level of *HLA-DR* was significantly ($P < 0.05$) high expressed in the *in vitro* polarized TAMs stimulated by the secretome of MCF7 and MDA-MB-231cells compared to SUM149 cells.

3.5. Gene enrichment analysis and PPI network construction

Through GeneMANIA analysis, we identified 20 neighboring genes with the highest frequency association with differential expressed macrophage polarization-related genes in each of *in vitro* polarized TAMs stimulated by the secretome of MCF7, MDA-MB-231, and SUM149 cells (Fig. 3A–C). These data indicate that *PTK2*, *IL10RA*, *CCR4*, *IFNAR2*, *CCL19*, *IRF5*, *ELP1*, *TLCD3A*, *HSD11B1*, *CCL17*, *HLA-DMB*, *SLC7A7*, *BSG*, *VCAM1*, *AJUBA*, *SAMHD1*, *LYVE1*, *SLC7A5*, *ADA* and *KDM8* neighboring genes were associated with the function and pathway of DEGs determined in gene expression analysis of *in vitro* polarized TAMs by the secretome of MCF7 cells. *HSP90AB1*, *SLC7A10*, *SLC7A7*, *LBP*, *SLC1A3*, *PKLR*, *IL10RA*, *SLC7A5*, *HLADRB1*, *VCAN*, *CEBPA*, *STAB1*, *VEGFB*, MMP13, *IL19*, *IL20*, *BAAT*, *CCR4*, *SLC1A1*, and *AGMAT* neighboring genes were associated with the function and pathway of DEGs determined in gene expression analysis of *in vitro* polarized TAMs by the secretome of MDA-MB-231 cells. *HSP90AB1*, *CTLA4*, *MARCHF8*, *VEGFB*, *CD28*, *A2M*, *PGF*, *SLC7A10*, *IL10RA*, *STAB1*, *SLC7A5*, *BAAT*, LBP, *SLC7A7*, *HLADRB1*, *IL19*, *IL20*, *TLR2*, *SLC3A1*, and *THBS1* neighboring genes were associated with the function and pathway of DEGs determined in gene expression analysis of *in vitro* polarized TAMs by the secretome of SUM19 cells. The functions of these DEGs and their neighboring genes were predicted using Metascape. The top 16 GO enrichment items of these DEGs and their neighboring genes focused on negative regulation of biological process, viral process, cellular process, metabolic process, signaling, biological process involved in interspecies interaction between organisms, localization, response to stimulus, locomotion, multicellular organismal process, positive regulation of biological process, developmental process, regulation of biological process, immune system process, biological regulation, and reproductive process (Fig. 3D).

Pathway enrichment analysis represented that response to extracellular stimulus, response to peptide, viral entry into host cell, cell activation, Network map of SARS-CoV-2 signaling pathway, positive regulation of protein phosphorylation, regulation of leukocyte migration, Allograft rejection, Tuberculosis, Interleukin-4 and Interleukin-13 signaling, negative regulation of immune system process, regulation of sprouting angiogenesis, L-alpha-amino acid transmembrane transport, Interleukin-10 signaling, cellular response to lipopolysaccharide, Orexin receptor pathway, response to inorganic substance, arginine metabolic process, COVID-19 adverse outcome pathway, and Prostaglandin signaling involved in TAMs polarization (Fig. 3E) (Table 2). The gene overlap analysis expanded *via* shared enriched ontologies was described in (Fig. 3F and G). Moreover, to better understand the relationship between DEGs and their neighboring genes, we then performed a Metascape protein-protein interaction (PPI) enrichment analysis. The PPI network and MCODE components are shown in (Fig. 3H–L).

3.6. Synchrotron infrared microspectroscopy single fixed cell analysis

3.6.1. FTIR spectral assignment of in vitro polarized TAMs

The mean representative spectra of the *in vitro* polarized TAMs stimulated by the secretome of MCF7, MDA-MB-231, and SUM149 cells demonstrate the typical features of biological cells. The averaged FTIR spectra display characteristic vibrational absorption bands of biological cells mainly the Amides I and II, as well as, the lipid region. As summarized in (Table 3), and depicted in (Fig. 4A), the following spectral signatures were observed among the studied monocytes as a sequence of peaks of different intensities in the region of 1500–1200 cm^{-1}. Very intense absorption bands in the region of 1700–1500 cm^{-1} are attributed to the amide I ν(C=O), & ν_{AS} (C—N), δ (N—H), and amide II ν(C—N), δ (N—H) proteins bands, with a strong broad signal in the 3600–3200 cm^{-1} related to the νN-H Amides A and B. In addition, three peaks of different intensities and areas were detected in the lipid region of the νCH_2 and νCH_3 stretching modes positioned within the 3000–2800 cm^{-1} range.

3.6.2. Curve fitting and second derivatives analysis

Precise information about the evolution of biological constituents such as proteins and lipids is very significant. The amide I band (1700–1600 cm^{-1}) has proven to be the most sensitive band commonly used to monitor the proteins' secondary structures [45]. In addition, the minima predicted by the second derivatives of the mean spectra are also involved to resolve the overlapped peaks of the Amide I band revealing information about the secondary structures such as α-helices, β-sheets, and β-turns among others. This highlights alterations in the composition of the protein presented by conformational changes, and/or possible folding states.

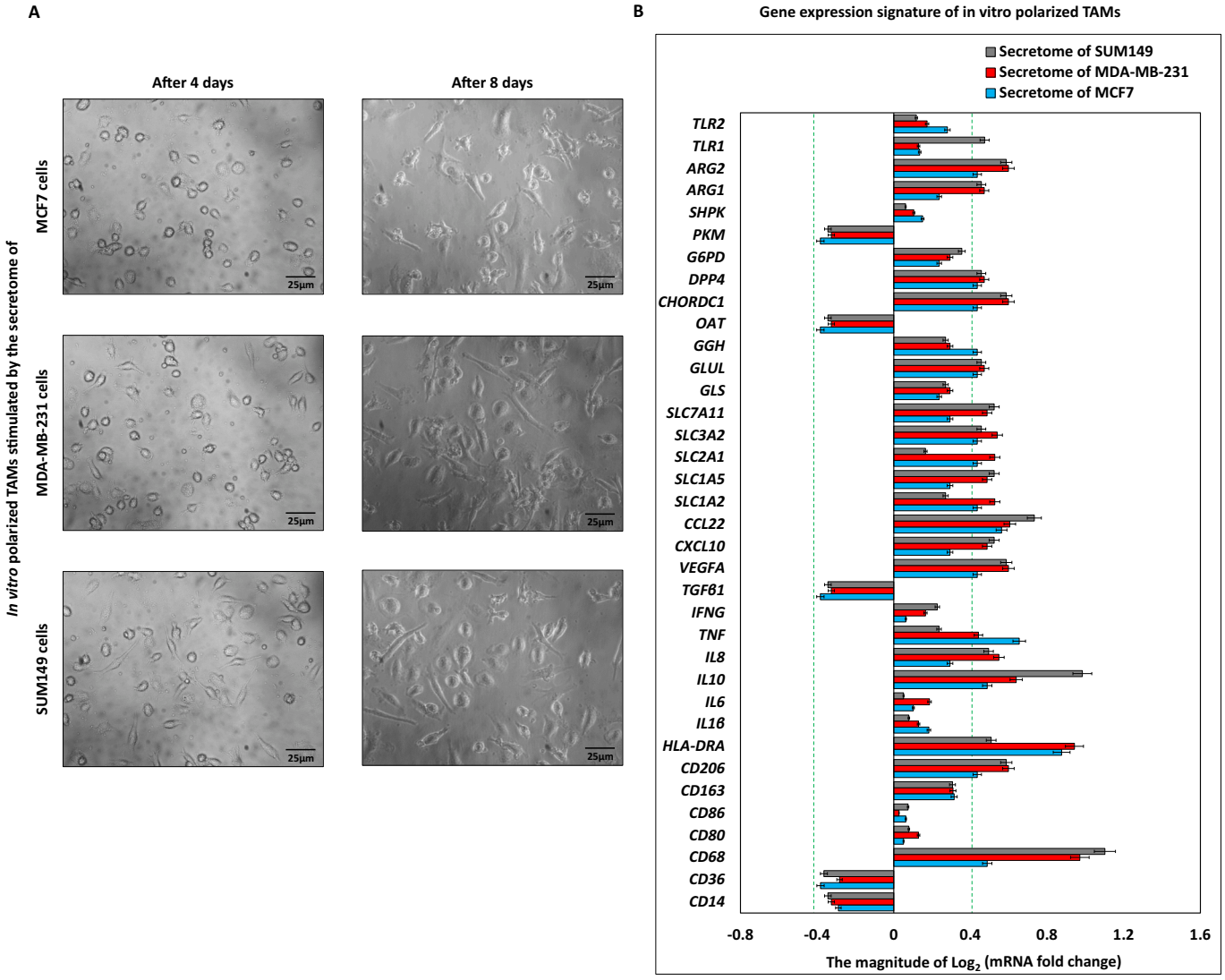

Fig. 2. Characterization of *in vitro* polarized TAMs *via* microscopic examination and quantitative Real-time PCR. (A) Microscopic images showed the polarization status of TME $CD14^+$ monocytes isolated from IBC and non-IBC patients, where (M0 macrophages) were identified as small/roundish cells without cytoplasmic projections on the cell surface, (M1 macrophages) were identified as enlarged amoeboid cells characterized by the presence of many delicate cytoplasmic extensions on the cell surface with visible intracellular vacuoles, and (M2 macrophages) were identified as a large and elongated "spindeloid" cells with cytoplasmic extensions on the apical ends of the cell bodies. (B) Clustered bars represent the mRNA expression of macrophage polarization-related genes of the *in vitro* polarized TAMs compared to mock cells. Data represented the mean of ±SD (number of experimental replicates = 3). $P < 0.05$ consider significant as determined by the one-way ANOVA test followed by Tukey's HSD and *Post Hoc* tests.

3.6.3. Amides I and II region (1700–1500 cm^{-1})

Curve-fitting was applied to decompose Amide I and II bands to their individual Gaussian components followed by secondary structure assignment. Relative percentages of the individual components were obtained, with the assumption that the overall sum of decomposed peaks' areas signifies the total amount of the secondary structures in the protein and as a result the conformational state. Second derivatives of the FTIR spectra have clearly demonstrated some differences between the three *in vitro* polarized TAMs. Similarities were noted mostly between the *in vitro* polarized TAMs stimulated by the secretome of MDA-MB-231 and SUM149 with respect to the *in vitro* polarized TAMs stimulated by the secretome of MCF7 cells (Fig. 4B and C). Additional investigation was done to assess the secondary structures' relative contribution to the whole area of the amides bands I and II as summarized in Table 4. *In vitro* polarized TAMs stimulated by the secretome of MCF7 cells, Amide I deconvolution indicated that the random coils secondary structure prevails over the parallel β-sheets and the β-turns. On the contrary, the β-sheets structure was found to be the major constituent in both the *in vitro* polarized TAMs stimulated by the secretome of MDA-MB-231 and SUM149 cells. Yet, both later *in vitro* polarized TAMs showed an intrinsic difference from each other: in the *in vitro* polarized TAMs stimulated by the secretome of SUM149, the β-sheets were found to be of higher percentage than both 3_{10} helices and β-turns, while in the *in vitro* polarized TAMs stimulated by the secretome of MDA-MB-231 cells, the β-sheets were found to prevail over both α-helices and β-turns. For the Amide II band, it was observed that the α-helix is more dominant than the random coils and β-turns for the *in vitro* polarized TAMs stimulated by the secretome of MCF7cells. In addition, again, the anti-parallel β-sheets were found to be prevalent over the α-helix secondary structure in both the *in vitro* polarized TAMs stimulated by the secretome of MDA-MB-231 and SUM149 cells.

3.6.4. Lipid absorption region (2800–3000 cm^{-1})

The lipid region is attributed to the phospholipid bilayer of cells and organelle membranes. Fatty acids are composed of repeated CH_2 and CH_3 chain moieties which are responsible for the asymmetric and

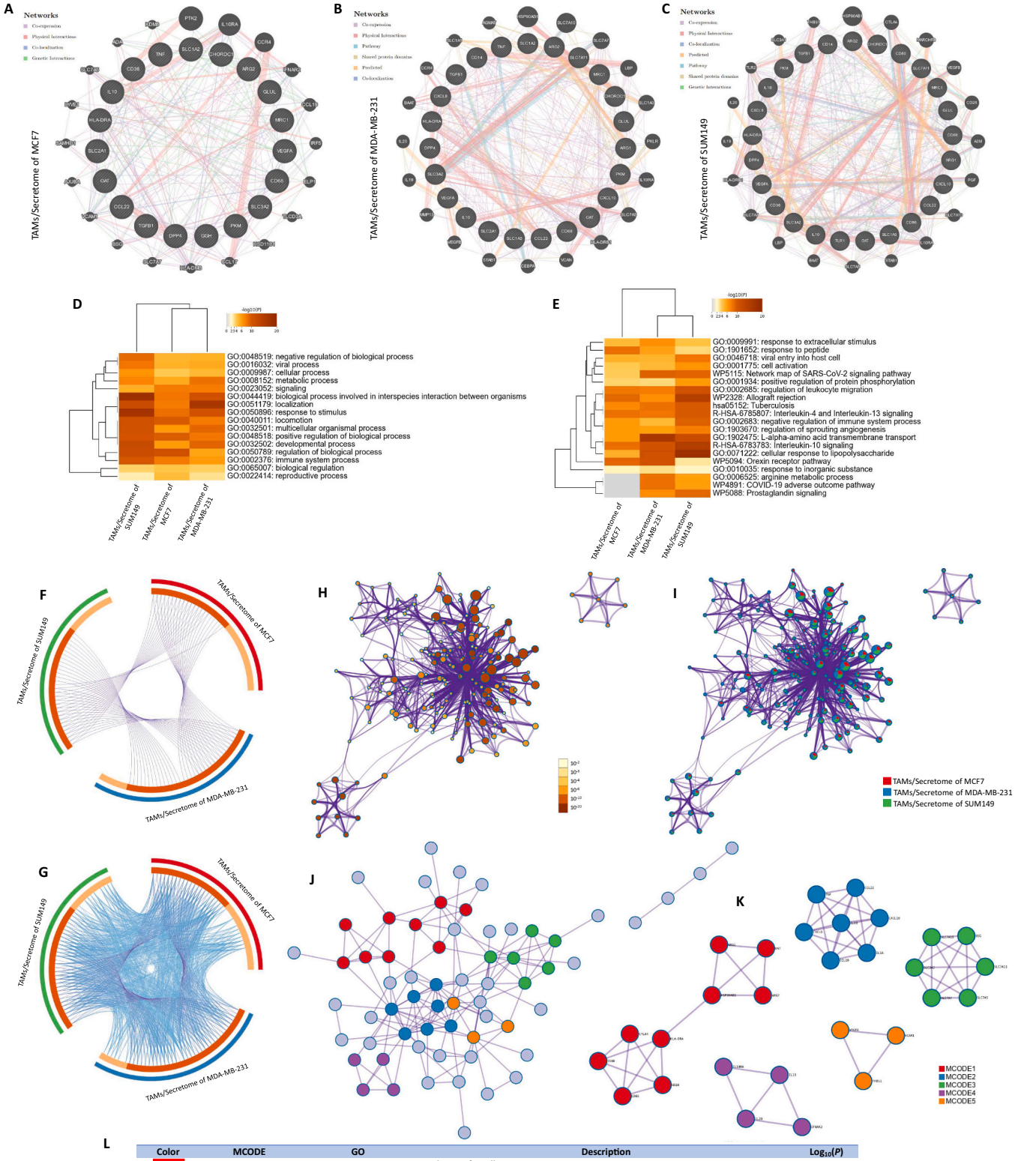

L

Color	MCODE	GO	Description	$Log_{10}(P)$
	MCODE_1	GO:0050863	regulation of T cell activation	-11.9
	MCODE_1	GO:1903037	regulation of leukocyte cell-cell adhesion	-11.9
	MCODE_1	hsa05320	Autoimmune thyroid disease	-11.8
	MCODE_2	R-HSA-6783783	Interleukin-10 signaling	-19.9
	MCODE_2	WP5095	Overview of proinflammatory and profibrotic mediators	-16.7
	MCODE_2	hsa04061	Viral protein interaction with cytokine and cytokine receptor	-14.1
	MCODE_3	R-HSA-210991	Basigin interactions	-18.8
	MCODE_3	R-HSA-352230	Amino acid transport across the plasma membrane	-14.2
	MCODE_3	R-HSA-202733	Cell surface interactions at the vascular wall	-14.1
	MCODE_4	hsa04630	JAK-STAT signaling pathway	-9.1
	MCODE_4	hsa04060	Cytokine-cytokine receptor interaction	-8
	MCODE_4	hsa04061	Viral protein interaction with cytokine and cytokine receptor	-6.9
	MCODE_5	M18	PID INTEGRIN1 PATHWAY	-8
	MCODE_5	GO:0001666	response to hypoxia	-6.1
	MCODE_5	GO:0036293	response to decreased oxygen levels	-6.1

(caption on next page)

Fig. 3. Gene enrichment analysis of DEGs obtained from different *in vitro* polarized TAMs gene expression signature analysis. (A–C) Gene-gene interaction network of different expressed macrophage polarization-related genes and their neighboring genes. Each node represents a gene, and the size of which represents the strength of the interaction. (D) Bar graph of the top-level Gene Ontology biological processes, colored by *P*-values. (E) Bar graph of enriched terms across input gene lists, colored by *P*-values. (F) Gene Overlap analysis, Circos plot shows how genes from the input gene lists overlap. On the outside, each arc represents the identity of each gene list, using the same color code as the color used in Table 2. On the inside, each arc represents a gene list, where each gene member of that list is assigned a spot on the arc. The dark orange color represents the genes that are shared by multiple lists and the light orange color represents genes that are unique to that gene list. Purple lines link the same gene that are shared by multiple gene lists. The greater the number of purple links and the longer the dark orange arcs imply greater overlap among the input gene lists. (G) Gene overlap analysis expanded *via* Shared Enriched Ontologies, Circos plot shows how genes from the input gene lists overlap. Purple lines link the same gene that are shared by multiple gene lists. Blue lines link the genes, although different, fall under the same ontology term (the term has to be statistically significantly enriched and with a size no larger than 100). The greater the number of purple links and the longer the dark orange arcs imply greater overlap among the input gene lists. Blue links indicate the amount of functional overlap among the input gene lists. (H and I) Network of enriched terms: firstly, colored by *p*-value, where terms containing more genes tend to have a more significant *P*-value; secondly pied by Gene Counts Across Studies, each pie sector is proportional to the number of hits originated from a gene list. Color code for pie sector represents a gene list and is consistent with the colors used in Table 2. (J and K) Protein-protein interaction network and MCODE components are identified in the gene list. (L) The table showed the functional analysis of MCODE1, MCODE2, MCODE3, and MCODE4 components.

Table 2
Gene enrichment analysis of DEGs obtained from different *in vitro* polarized TAMs gene expression signature analysis.

Pattern	GO	Category	Description	Count	%	$Log_{10}(P)$	$Log_{10}(q)$
	GO:0071222	GO Biological Processes	Cellular response to lipopolysaccharide	13	30.23	−18.01	−13.66
	WP2328	WikiPathways	Allograft rejection	12	16.9	−17.66	−13.5
	R-HSA-6783783	Reactome Gene Sets	Interleukin-10 signaling	10	14.08	−16.89	−13.02
	GO:1902475	GO Biological Processes	L-alpha-amino acid transmembrane transport	9	21.95	−16.21	−12.64
	GO:0002685	GO Biological Processes	Regulation of leukocyte migration	14	19.72	−15.91	−12.45
	WP5094	WikiPathways	Orexin receptor pathway	10	14.08	−11.48	−8.91
	R-HSA-6785807	Reactome Gene Sets	Interleukin-4 and Interleukin-13 signaling	9	12.68	−11.37	−8.82
	hsa05152	KEGG Pathway	Tuberculosis	10	14.08	−10.83	−8.34
	GO:0002683	GO Biological Processes	Negative regulation of immune system process	13	18.31	−10.64	−8.17
	GO:1901652	GO Biological Processes	Response to peptide	13	18.31	−10.51	−8.07
	WP5088	WikiPathways	Prostaglandin signaling	6	8.45	−9.84	−7.45
	WP5115	WikiPathways	Network map of SARS-CoV-2 signaling pathway	8	19.51	−9.25	−6.89
	GO:0001934	GO Biological Processes	Positive regulation of protein phosphorylation	14	19.72	−8.77	−6.44
	GO:0001775	GO Biological Processes	Cell activation	13	18.31	−8.48	−6.2
	WP4891	WikiPathways	COVID-19 adverse outcome pathway	4	9.76	−8.4	−6.19
	GO:0006525	GO Biological Processes	Arginine metabolic process	4	9.76	−8.28	−6.08
	GO:0046718	GO Biological Processes	Viral entry into host cell	7	9.86	−8.23	−5.98
	GO:0009991	GO Biological Processes	Response to extracellular stimulus	11	15.49	−7.81	−5.64
	GO:1903670	GO Biological Processes	Regulation of sprouting angiogenesis	5	11.63	−7.62	−5.55
	GO:0010035	GO Biological Processes	Response to inorganic substance	11	15.49	−7.44	−5.31

Table 3
Amide I and Amide II, and lipids FTIR spectral peaks assignment.

In vitro polarized TAMs stimulated by the secretome of			FTIR spectral peaks assignment
MCF7	MDA-MB-231	SUM149	
3290	3290	3284	NH asymmetric stretching (proteins), Amide A
3084	3078	3074	Alkene (=C-H) stretching
2959	2958	2957	CH_3 asymmetric stretching
2927	2923	2923	CH_2 asymmetric stretching
2876	–	–	CH_3 symmetric stretching
–	2854	2854	CH_2 symmetric stretching
1649	1635	1646	Amide I
1535	1529	1530	Amide II
1452	1474	1452	CH_3 asymmetric stretching of proteins
1394	1411	1412	CH_3 symmetric stretching of proteins
1374	1383	1377	Methyl C—H rocking
–	1329	–	–
1313	1304	1310	CH_2 stretching (phospholipids)
1272	1233	1236	PO_2 asymmetric stretching (DNA/RNA), Amide III
1203	–	–	–

symmetric stretching vibration of the main lipid region. Together with the protein signatures, the lipid profile of the modern skin sample was identified by monitoring the lipid sequence within the spectral window 3000–2800 cm^{-1}. In this region, and as detected from the second derivative of the *in vitro* polarized TAMs spectra, a sequence of small peaks or shoulders was noted due to antisymmetric and symmetric stretching of the long hydrocarbon chains that are related to lipids such as ceramides, phospholipids, or glycolipids. The curve-fitting applied to the lipid vibrational region (3000–2800 cm^{-1}) depicts the individual Gaussian components with a clear variation between the three *in vitro* polarized TAMs as described in (Fig. 4D and E) and Table 5.

3.6.5. Multivariate Statistical Analysis (MVA)

Multivariate Analysis (MVA) was applied to distinguish the spectra based on biochemical similarities and differences in lipids, and protein secondary structures of the three groups of cells. The Principal Component Analysis, PCA, was performed on the lipid region of the FTIR spectra and the second derivative spectra of the amide region using the NIPALS (Non-linear Iterative Partial Least Squares) algorithm. In principle, PCA is performed to decrease the dimensionality by obtaining a small group of principal components (PC) able to describe the most variability within the dataset. PCA analysis of the lipid and amide regions was able to separately differentiate between the spectra of different cell lines, as shown in the score plots presented in (Fig. 5). In

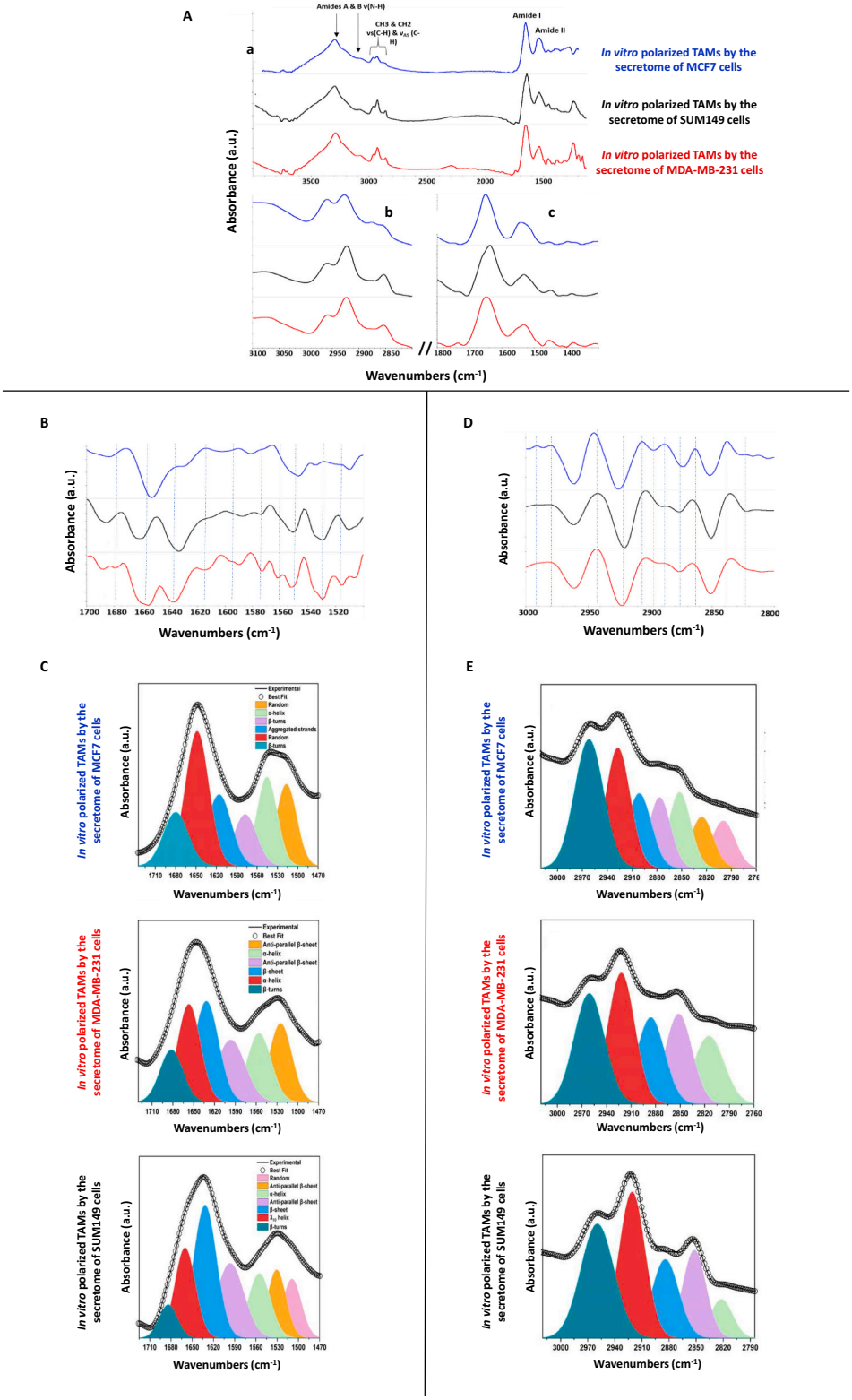

Fig. 4. FTIR spectral assignment of *in vitro* polarized TAMs. (A) Normalized mean absorbance spectra (average of 15 spectra for each cell type) of *in vitro* polarized TAMs stimulated by the secretome of MCF7 (Blue), MDA-MB-231 (Red), and SUM149 (Black) cells, the lipids regions (3000–2800 cm^{-1}), and the proteins absorption region (1700–1500 cm^{-1}). (B) Differences in the proteins absorption region (1700–1500 cm^{-1}) as detected for the *in vitro* polarized TAMs stimulated by the secretome of MCF7 (Blue), MDA-MB-231 (Red), and SUM149 (Black) cells, based on their second derivatives. Dashed lines are indicating the visual differences between the three *in vitro* polarized TAMs. (C) Curve fitting assignment considering the Amides I and II vibrational bands of the *in vitro* polarized TAMs stimulated by the secretome of MCF7, MDA-MB-231, and SUM149 cells. (D) Differences in the lipids region (2800–3000 cm^{-1}) as detected for the *in vitro* polarized TAMs stimulated by the secretome of MCF7 (Blue), MDA-MB-231 (Red), and SUM149 (Black) cells, based on their second derivatives. Dashed lines are indicating the visual differences between the three *in vitro* polarized TAMs. (E) Curve fitting assignment considering the lipid vibrational bands of the *in vitro* polarized TAMs stimulated by the secretome of MCF7, MDA-MB-231, and SUM149 cells. All spectra are offset displayed for clarity. (Number of experimental replicates = 5).

the PCA scores plot of the second derivative mean spectra (n = 5) (Average of 15 spectra of 5 experimental replicates) of the amide region (Fig. 5A and B), the PCA model was able to explain 77 % of the variance, with 63 % explained by PC1 and 14 % explained by PC2. As seen in the plot, there is significant inter-cluster heterogeneity between the spectra of *in vitro* polarized TAMs stimulated by the secretome of MCF7 cells, and those of both *in vitro* polarized TAMs stimulated by the secretome of MDA-MB-231 and SUM149 cells. The scores of *in vitro* polarized TAMs stimulated by the secretome of MCF7 cells spectra are clustered in the positive part of the PC1 axis and vary along PC2, being distributed between the positive and negative part of its axis. On the other hand, the scores of *in vitro* polarized TAMs stimulated by the secretome of MDA-MB-231 and SUM149 cells spectra are clustered in the negative part of the PC1 axis, but vary along with the positive and negative parts of the

Table 4
Protein secondary structures assignment for Amide I and Amide II second derivatives spectra.

In vitro polarized TAMs stimulated by the secretome of	Amide I			Amide II		
	Peak	%	Secondary structure assignment	Peak	%	Secondary structure assignment
MCF7	1616	27.9	Agg. Strnds./ parallel β sheets	1517	35.8	Random coils
	1648	50.7	Random coils	1545	38.8	α helix
	1680	21.4	β turns	1578	25.4	β turns
	β turns < Strnds./parallel β sheets < Random coils			β turns < Random coils < α helix		
MDA-MB-231	1632	42	β sheets	1525	34	Anti.p. β sheets
	1657	37.8	α helix	1556	32	α helix
	1682	20.2	β turns	1597	34	Anti.p. β sheets
	β turns < α helix < β sheets			α helix < Anti.p. β sheets		
SUM149	1632	55.6	β sheets	1509	19.2	Random coils
	1660	33.6	3_{10} helix	1531	21.6	Anti.p. β sheets
	1684	10.8	β turns	1555	24.4	α helix
				1596	34.8	Anti.p. β sheets
	β turns < 3_{10} helix < β sheets			Random coils < α helix < Anti. p. β sheets		

Table 5
Individual components as obtained from the second derivatives spectra of lipid.

In vitro polarized TAMs stimulated by the secretome of		
MCF7	MDA-MB-231	SUM149
2800	–	–
2826	2815	2822
2852	2852	2852
2877	2885	2884
2901	–	–
2927	2922	2921
2962	2961	2960

PC2 axis. The scores of *in vitro* polarized TAMs stimulated by the secretome of MDA-MB-231 and SUM149 cells spectra display low inter-cluster heterogeneity with each other. In the scores plot of the second derivative mean spectra ($n = 5$) (Average of 15 spectra of 5 experimental replicates) of the lipid region, the PCA model was able to explain a total of 92 % of the variance with PC1 explaining 72 % and PC2 explaining 20 % (Fig. 5C and D). The scores of *in vitro* polarized TAMs stimulated by the secretome of MCF7 cells spectra are clustered along the negative part of the PC1 axis and the positive part of the PC2 axis, with the scores varying more along PC1 with less variation along PC2. The scores of the spectra of *in vitro* polarized TAMs stimulated by the secretome of MDA-MB-231 cells are scattered along with the positive and negative parts of both PC1 and PC2 axes, yet they show more variability along PC1. The spectra of *in vitro* polarized TAMs stimulated by the secretome of SUM149 cells showed the highest variability among the three groups between its spectra, being remarkably scattered along with the positive and negative parts of both PC1 and PC2 axes. The within-cluster heterogeneity of the spectra of *in vitro* polarized TAMs stimulated by the secretome of MCF7cells is less than that of MDA-MB-231 and SUM149 spectra.

4. Discussion

Vibrational microspectroscopy and imaging is a highly sensitive analytical tool with various apparent advantages in the cancer diagnosis field [18]. It has the potential to detect any molecular modifications before any morphological changes. These determined spectroscopic modifications are associated with any changes in the concentration and the conformational orientation of functional groups related to proteins, lipids, nucleic acids, and carbohydrates. The time between diagnosis and the decision of starting treatment can be very long and distressing for cancer patients and the cost is very substantial for health care. Vibrational spectroscopy, as a 'spectral histological' method for cancer diagnosis and prognosis, can be used as a screening method to help histopathologists in their selection and accordingly shorten the delay time. A strong correlation between gene expression patterns and FTIR spectral information has been verified for 13 breast cancer cell lines grown in 2D and 3D culture conditions [46]. Mohamed and colleagues applied vibrational microspectroscopy with chemometric analysis tools to identify IBC and non-IBC at cell and tissue levels [17].

Single-cell technology plays a pivotal role in cancer research. Recently, single-cell research has advanced to the point that it can now identify rare forms of cancer cells such as circulating tumor cells and cancer stem cells. It also gave the researchers the ability to study intratumor heterogeneity and tumor epigenetics [47] and identify the differences in the cellular composition between normal and malignant human colon epithelia [48]. Single-cell RNA sequencing was used by Patel and colleagues to investigate different transcriptional programs of cancer cells obtained from five primary glioblastomas [49]. To study the heterogeneity within leukemic cells, single-cell analysis was also employed by Saadatpour and colleagues using the MLL-AF9 driven mouse model of acute myeloid leukemia [50]. In the field of breast cancer research, different aspects of single-cell technology have also been applied to study the intracellular heterogeneity of breast cancer cells, cell-cell communications as well as identifying drug targets thus facilitating individualized therapy [51]. Single-cell sequencing technology has been applied to study the progression from *in situ* to invasive breast cancer [52]. Casasent and colleagues also cast topographic single-cell sequencing to study genetic mutations and aberrations in ductal carcinoma *in situ* before the invasion of adjacent tissues and progressing into invasive carcinomas [53].

FTIR microspectroscopy using synchrotron radiation rather than the thermal source is a tremendous achievement in the field of clinical research, which helped in taking the analysis down to the cellular and subcellular levels in studying different diseases including breast cancer [54]. SR-μFTIR was used to study the antiproliferative activity of the combination of a chemotherapy drug with a natural antioxidant on the MCF7 breast cancer cell line [55]. SR-μFTIR was also implemented to study the molecular changes associated with chronic oxidative stress in basal and luminal mammary epithelial cells and the stroma of breast tissues [56]. SR-μFTIR and imaging analyses were used to investigate inflammatory and non-inflammatory breast cancer single cells, and their GAGs and proteoglycans in an attempt to provide a discrimination tool between inflammatory and non-inflammatory breast cancer cell lines [57]. Attenuated total reflection SR-FTIR was used in studying the primary pharmacological target of an anticancer drug as well as studying its effect on the DNA extracted from MDA-MB-231 breast cancer cells [58].

In the present study, we determine the incidence of $MAC387^+$ TAMs in the cancer tissues of IBC and non-IBC patients. The IHC analysis showed that the IBC cancer tissues were characterized by a significantly high incidence of $MAC387^+$ TAMs compared to non-IBC cancer tissues. In addition, the immunophenotyping analysis showed nonsignificantly high infiltration of $CD14^+$, $CD16^+$, and $HLA\text{-}DR^+$ mononuclear cells in the TME blood collected from IBC compared to non-IBC patients. Previously, we found that $CD14^+$ cells highly infiltrate the tumor microenvironment of IBC compared to non-IBC patients [59]. High incidence of migratory $MAC387^+$ TAMs correlated with aggressiveness and worse outcomes in breast cancer [44]. The incidence of $MAC387^+$ TAMs was associated with high-grade, HR-negative breast cancers and early

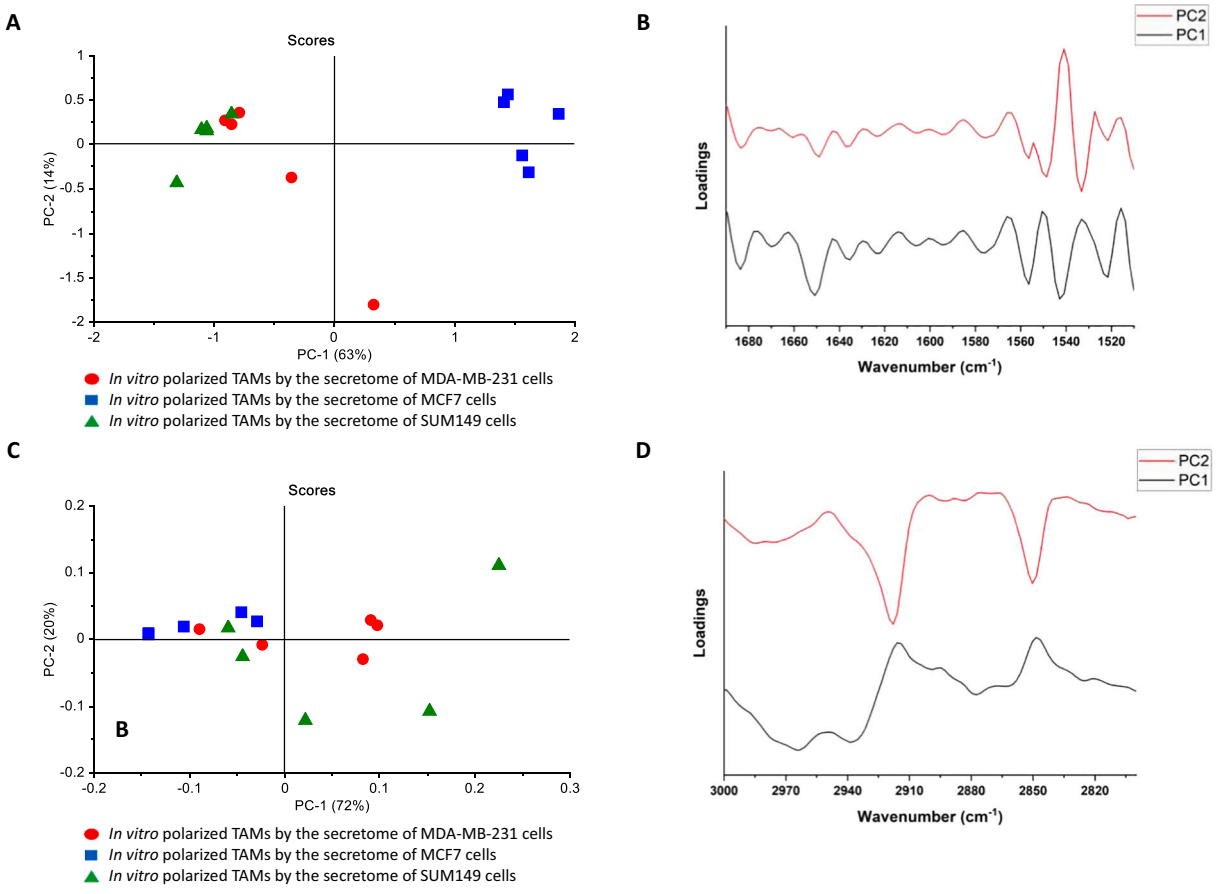

Fig. 5. The Principal Component Analysis for the amide and lipid region of the obtained FTIR spectra of the *in vitro* polarized TAMs stimulated by the secretome of MCF7 (Blue square), MDA-MB-231 (Red circle), and SUM149 (Green triangle) cells using NIPALS (Non-linear Iterative Partial Least Squares) algorithm. (A and B) PCA scores and loadings' plots of the second derivative spectra ($n = 5$) of the amide region. (C and D) PCA scores and loadings' plots of the second derivative spectra (n = 5) of the Lipid region. Each spectrum from the five spectra for each cell type represents the mean spectra of three statistical replicates for each experimental replicate (Number of experimental replicates = 5).

recurrence [44,60,61]. It was demonstrated that MAC387 was expressed by a subset of TAMs as well as by a subset of cancer cells as a result of the fusion between TAMs and cancer cells leading to an increase in disease aggressiveness [62–64]. Tumor-infiltrated monocytes isolated from IBC and non-IBC TME blood were *in vitro* polarized into TAMs after stimulation by the secretome of MCF7, MDA-MB-231, and SUM149 cells. The microscopic examination and transcriptome analysis showed that the secretome of MCF7, MDA-MB-231, and SUM149 cells was able to polarize tumor-infiltrating monocytes into M1/M2 TAMs *in vitro*. Benner and colleagues demonstrated that TAMs stimulated by conditioned media of MDA-MB-231 cells displayed an increase in the co-expression of CD163/CD206 compared to *in vitro* M2-like macrophages [65]. Indeed, these generated *in vitro* TAMs exhibited high transcriptional levels of IL-6, IL-10, CCL2, c-Myc, iNOS, and arginase compared to *in vitro* M2-like macrophages [65]. To better understand of the role of differentially expressed macrophage polarization-related genes among *in vitro* polarized TAMs stimulated by the secretome of IBC and non-IBC cells, multiple gene list enrichment analyses, and PPI network construction were done. The Pathway enrichment analysis showed that cellular response to lipopolysaccharide, Allograft rejection, Interleukin-10 signaling, L-alpha-amino acid transmembrane transport, regulation of leukocyte migration, Orexin receptor pathway, Interleukin-4, and Interleukin-13 signaling, Tuberculosis, negative regulation of immune system process, response to peptide, Prostaglandin signaling, Network map of SARS-CoV-2 signaling pathway, positive regulation of protein phosphorylation, cell activation, COVID-19 adverse outcome pathway, arginine metabolic process, viral entry into host cell, response to extracellular stimulus, regulation of sprouting angiogenesis, and response to inorganic substance were involved in polarization process in TAMs.

In addition, the SR-μFTIR technique was applied to recognize the intracellular biochemical changes which can provide cellular spectral markers allowing the differentiation between TAMs subtypes within IBC and non-IBC TME independently on surface markers or secreted cytokines and chemokines. Previous studies indicated that TAMs in both non-IBC and IBC TME were belonging to the M2c macrophage subtype depending on their surface marker and secreted cytokines [66,67]. However, the effect of the aggressive IBC cells on the polarization status of tumor-infiltrated monocytes may be different from the non-IBC cells. MVA Analysis was applied to distinguish the spectra based on biochemical similarities and differences in lipids, and protein secondary structures of the three *in vitro* polarized TAMs. The PCA analysis of the second derivative spectra of the amide region showed significant inter-cluster heterogeneity between the spectra of the three *in vitro* polarized TAMs stimulated by the secretome of MCF7, MDA-MB-231, and SUM149 cells. The PC-1/PC-2 carried 77 % of the variance and PC1 was able to discriminate between the *in vitro* polarized TAMs by the secretome of MCF7 cells from the other TMAs groups. In the PCA analysis of the lipid region, the within-cluster heterogeneity of the spectra of *in vitro* polarized TAMs stimulated by the secretome of MCF7cells is less than that of MDA-MB-231 and SUM149 spectra. PC-1/PC-2 carried 92 % of the variance and both PCs were unable to discriminate between the three *in vitro* polarized TAMs stimulated by the secretome of MCF7, MDA-MB-231, and SUM149 cells. This can suggest that spectra of the amide

region can be used to easily discriminate between the TAMs in the IBC and non-IBC TME.

5. Conclusions

This study is the first study to apply the SR-μFTIR technique to characterize *in vitro* polarized TAMs by the secretome of IBC and non-IBC cells. The obtained results showed that there is a different effect of IBC and non-IBC cells on the polarization status of tumor-infiltrated monocytes inside the TME and SR-μFTIR enabled us to discriminate between different *in vitro* stimulated TAMs independently from morphological changes. From this, we may know the different potential roles of TAMs populations in both non-IBC and IBC TME.

CRediT authorship contribution statement

Hossam Taha Mohamed: Methodology, Validation, Writing – original draft, Supervision. **Gihan Kamel:** Validation, Formal analysis, Writing – original draft. **Noura El-Husseiny:** Methodology. **Aya Ali El-Sharkawy:** Methodology. **Ahmed A. El-Sherif:** Supervision. **Mohamed El-Shinawi:** Resources, Writing – review & editing, Supervision. **Mona Mostafa Mohamed:** Validation, Writing – original draft, Supervision.

Declaration of competing interest

The authors declare that they have no known competing financial interests or personal relationships that could have appeared to influence the work reported in this paper.

Data availability

There are no restrictions on the availability of the presented materials, data, and associated protocols.

Acknowledgments

This work was conducted in the Cancer Biology Research Laboratory, Faculty of Science, Cairo University, Egypt, and SESAME Synchrotron, Alan, Jordan. Special thanks to Egyptian breast cancer patients who participated in the present study.

Funding

The study was supported by the Cairo University Scientific Research Sector (MMM), Avon Foundation Grants # 02-2009-085 a and b (MMM) and SESAME Synchrotron (HTM).

Ethics approval

The study protocol was approved by the Institutional Review Board (IRB#00006379), Faculty of Medicine, Ain Shams University, Egypt. Before participation, all patients signed consent forms, including approval for publication of the study results.

References

[1] M.J. Hashim, F.A. Al-Shamsi, N.A. Al-Marzooqi, S.S. Al-Qasemi, A.H. Mokdad, G. Khan, Burden of breast cancer in the Arab world: findings from global burden of disease, J. Epidemiol. Glob. Health 8 (2018) (2016) 54–58.
[2] X. Jin, P. Mu, Targeting breast cancer metastasis, Breast Cancer 9 (2015) 23–34.
[3] M.M. Mohamed, D. Al-Raawi, S.F. Sabet, M. El-Shinawi, Inflammatory breast cancer: new factors contribute to disease etiology: a review, J. Adv. Res. 5 (2014) 525–536.
[4] A. Huang, S. Cao, L. Tang, The tumor microenvironment and inflammatory breast cancer, J. Cancer 8 (2017) 1884–1891.
[5] J.M. Matro, T. Li, M. Cristofanilli, M.E. Hughes, R.A. Ottesen, J.C. Weeks, Y. N. Wong, Inflammatory breast cancer management in the national comprehensive cancer network: the disease, recurrence pattern, and outcome, Clin. Breast Cancer 15 (2015) 1–7.
[6] M.Di Bonito, M. Cantile, G.J.T.C.R. Botti, in: Pathological and Molecular Characteristics of inflammatory Breast Cancer, 2019, 2019, pp. S449–S456.
[7] Z. Ge, S. Ding, The Crosstalk Between Tumor-associated Macrophages (TAMs) and Tumor Cells and the Corresponding Targeted Therapy 10, 2020.
[8] A. Mantovani, B. Bottazzi, F. Colotta, S. Sozzani, L. Ruco, The origin and function of tumor-associated macrophages, Immunol. Today 13 (1992) 265–270.
[9] T. Palaga, W. Wongchana, P. Kueanjinda, Notch signaling in macrophages in the context of cancer immunity, Front. Immunol. 9 (2018) 652.
[10] U. Juhas, M. Ryba-Stanisławowska, P. Szargiej, J. Myśliwska, Different pathways of macrophage activation and polarization, Postepy Hig. Med. Dosw (Online) 69 (2015) 496–502.
[11] O.V.Orekhov AN, N.G. Nikiforov, V.A. Myasoedova, A.V. Grechko, E. B. Romanenko, D. Zhang, D.A. Chistiakov, Monocyte differentiation and macrophage polarization, Vessel Plus 2 (2019) 20.
[12] C.D. Mills, M1 and M2 macrophages: oracles of health and disease, Crit. Rev. Immunol. 32 (2012) 463–488.
[13] J. Condeelis, J.W. Pollard, Macrophages: obligate partners for tumor cell migration, invasion, and metastasis, Cell 124 (2006) 263–266.
[14] R.J. Morrow, N. Etemadi, B. Yeo, M. Ernst, Challenging a misnomer? The role of inflammatory pathways in inflammatory breast cancer, Mediat. Inflamm. 2017 (2017) 4754827.
[15] R. Wang, Y. Wang, Fourier transform infrared spectroscopy in oral cancer diagnosis, Int. J. Mol. Sci. 22 (2021).
[16] H.T. Mohamed, V. Untereiner, G.D. Sockalingum, S. Brezillon, Implementation of infrared and raman modalities for glycosaminoglycan characterization in complex systems, Glycoconj. J. 34 (2017) 309–323.
[17] H.T. Mohamed, V. Untereiner, I. Proult, S.A. Ibrahim, M. Gotte, M. El-Shinawi, M. M. Mohamed, G.D. Sockalingum, S. Brezillon, Characterization of inflammatory breast cancer: a vibrational microspectroscopy and imaging approach at the cellular and tissue level, Analyst 143 (2018) 6103–6112.
[18] H.T. Mohamed, V. Untereiner, G. Cinque, S.A. Ibrahim, M. Gotte, N.Q. Nguyen, R. Rivet, G.D. Sockalingum, S. Brezillon, Infrared microspectroscopy and imaging analysis of inflammatory and non-inflammatory breast cancer cells and their GAG secretome, Molecules 25 (2020).
[19] S. Kumar, T.S. Shabi, E. Goormaghtigh, A FTIR imaging characterization of fibroblasts stimulated by various breast cancer cell lines, PLoS One 9 (2014) e111137.
[20] M.A. Nouh, M.M. Mohamed, M. El-Shinawi, M.A. Shaalan, D. Cavallo-Medved, H. M. Khaled, B.F. Sloane, Cathepsin B: a potential prognostic marker for inflammatory breast cancer, J. Transl. Med. 9 (2011) 1.
[21] M. El-Shinawi, H.T. Mohamed, E.A. El-Ghonaimy, M. Tantawy, A. Younis, R. J. Schneider, M.M. Mohamed, Human cytomegalovirus infection enhances NF-kappaB/p65 signaling in inflammatory breast cancer patients, PLoS One 8 (2013), e55755.
[22] M.M. Mohamed, S. Sabet, D.F. Peng, M.A. Nouh, M. El-Shinawi, W. El-Rifai, Promoter hypermethylation and suppression of glutathione peroxidase 3 are associated with inflammatory breast carcinogenesis, Oxidative Med. Cell. Longev. 2014 (2014), 787195.
[23] M. El-Shinawi, H.T. Mohamed, H.H. Abdel-Fattah, S.A. Ibrahim, M.S. El-Halawany, M.A. Nouh, R.J. Schneider, M.M. Mohamed, Inflammatory and non-inflammatory breast cancer: a potential role for detection of multiple viral DNAs in disease progression, Ann. Surg. Oncol. 23 (2016) 494–502.
[24] M. El-Shinawi, S.F. Abdelwahab, M. Sobhy, M.A. Nouh, B.F. Sloane, M. M. Mohamed, Capturing and characterizing immune cells from breast tumor microenvironment: an innovative surgical approach, Ann. Surg. Oncol. 17 (2010) 2677–2684.
[25] F. Heinrich, A. Lehmbecker, B.B. Raddatz, K. Kegler, A. Tipold, V.M. Stein, A. Kalkuhl, U. Deschl, W. Baumgärtner, R. Ulrich, I. Spitzbarth, Morphologic, phenotypic, and transcriptomic characterization of classically and alternatively activated canine blood-derived macrophages in vitro, PloS one 12 (2017) e0183572.
[26] J. Shi, Q. Li, M. Sheng, M. Zheng, M. Yu, L. Zhang, The role of TLR4 in M1 macrophage-induced epithelial-mesenchymal transition of peritoneal mesothelial cells, Cell. Physiol. Biochem. 40 (2016) 1538–1548.
[27] M. Orecchioni, Y. Ghosheh, A.B. Pramod, K. Ley, Macrophage Polarization: Different Gene Signatures in M1(LPS+) vs. Classically and M2(LPS–) vs. Alternatively Activated Macrophages 10, 2019.
[28] N. Eissa, H. Hussein, J.E. Ghia, A gene expression analysis of M1 and M2 polarized macrophages, Methods Mol. Biol. 2184 (2020) 131–144.
[29] D. Unuvar Purcu, A. Korkmaz, S. Gunalp, D.G. Helvaci, Y. Erdal, Y. Dogan, A. Suner, G. Wingender, D. Sag, Effect of stimulation time on the expression of human macrophage polarization markers, PLoS One 17 (2022), e0265196.
[30] P.J. Murray, in: Macrophage Polarization 79, 2017, pp. 541–566.
[31] A. Palma, A.S. Jarrah, P. Tieri, G. Cesareni, F. Castiglione, Gene regulatory network modeling of macrophage differentiation corroborates the continuum hypothesis of polarization states, Front. Physiol. 9 (2018) 1659.
[32] F.O. Martinez, S. Gordon, M. Locati, A. Mantovani, Transcriptional profiling of the human monocyte-to-macrophage differentiation and polarization: new molecules and patterns of gene expression, J. Immunol. 177 (2006) 7303–7311.
[33] Y. Zhao, M. Li, Y. Yang, T. Wu, Q. Huang, Q. Wu, C. Ren, Identification of macrophage polarization-related genes as biomarkers of chronic obstructive pulmonary disease based on bioinformatics analyses, Biomed. Res. Int. 2021 (2021) 9921012.
[34] C. Geiß, G. Alanis-Lobato, M. Andrade-Navarro, A. Régnier-Vigouroux, Assessing the reliability of gene expression measurements in very-low-numbers of human monocyte-derived macrophages, Sci. Rep. 9 (2019) 17908.

[35] M.W. Pfaffl, A new mathematical model for relative quantification in real-time RT-PCR, Nucleic Acids Res. 29 (2001), e45.
[36] T. Wang, Y. Zhang, J. Bai, Y. Xue, Q. Peng, MMP1 and MMP9 are potential prognostic biomarkers and targets for uveal melanoma, BMC Cancer 21 (2021) 1068.
[37] M. Li, M. He, F. Xu, Y. Guan, J. Tian, Z. Wan, H. Zhou, M. Gao, T. Chong, Abnormal expression and the significant prognostic value of aquaporins in clear cell renal cell carcinoma, PloS One 17 (2022) e0264553.
[38] Y. Jin, Q. Lin, H. Fei, L. Xue, L. Li, Q. Xi, H. Jiang, Bioinformatics analysis of potential therapeutic targets and prognostic biomarkers amid CXC chemokines in ovarian carcinoma microenvironment, J. Oncol. 2021 (2021) 8859554.
[39] A. Ota, S.-H. Hyon, S. Sumi, K. Matsumura, Gene expression analysis of human induced pluripotent stem cells cryopreserved by vitrification using StemCell keep, Biochem. Biophys. Rep. 28 (2021) 101172.
[40] G. Kamel, S. Lefrançois, M. Al-Najdawi, T. Abu-Hanieh, I. Saleh, Y. Momani, P. Dumas, EMIRA: the infrared synchrotron radiation beamline at SESAME, Synchrotron. Radiat. News 30 (2017) 8–10.
[41] G. Kamel, S. Lefrancois, T. Moreno, M. Al-Najdawi, Y. Momani, A. Abbadi, G. Paolucci, P. Dumas, The first infrared beamline at the Middle East SESAME synchrotron facility, J. Synchrotron. Radiat. 28 (2021) 1927–1934.
[42] S.B. Edge, C.C. Compton, The American Joint Committee on Cancer: the 7th edition of the AJCC cancer staging manual and the future of TNM, Ann. Surg. Oncol. 17 (2010) 1471–1474.
[43] P.B. Vermeulen, K.L. van Golen, L.Y. Dirix, Angiogenesis, lymphangiogenesis, growth pattern, and tumor emboli in inflammatory breast cancer: a review of the current knowledge, Cancer 116 (2010) 2748–2754.
[44] R.A. Mukhtar, A.P. Moore, V.J. Tandon, O. Nseyo, P. Twomey, C.A. Adisa, N. Eleweke, A. Au, F.L. Baehner, D.H. Moore, M.S. McGrath, O.I. Olopade, J. W. Gray, M.J. Campbell, L.J. Esserman, Elevated levels of proliferating and recently migrated tumor-associated macrophages confer increased aggressiveness and worse outcomes in breast cancer, Ann. Surg. Oncol. 19 (2012) 3979–3986.
[45] A. Sadat, I.J. Joye, in: Peak Fitting Applied to Fourier Transform Infrared and Raman Spectroscopic Analysis of Proteins 10, 2020, p. 5918.
[46] M. Smolina, E. Goormaghtigh, Gene expression data and FTIR spectra provide a similar phenotypic description of breast cancer cell lines in 2D and 3D cultures, Analyst 143 (2018) 2520–2530.
[47] S.-B. Liang, L.-W. Fu, Application of single-cell technology in cancer research, Biotechnol. Adv. 35 (2017) 443–449.
[48] P. Dalerba, T. Kalisky, D. Sahoo, P.S. Rajendran, M.E. Rothenberg, A.A. Leyrat, S. Sim, J. Okamoto, D.M. Johnston, D. Qian, M. Zabala, J. Bueno, N.F. Neff, J. Wang, A.A. Shelton, B. Visser, S. Hisamori, Y. Shimono, M. van de Wetering, H. Clevers, M.F. Clarke, S.R. Quake, Single-cell dissection of transcriptional heterogeneity in human colon tumors, Nat. Biotechnol. 29 (2011) 1120–1127.
[49] A.P. Patel, I. Tirosh, J.J. Trombetta, A.K. Shalek, S.M. Gillespie, H. Wakimoto, D. P. Cahill, B.V. Nahed, W.T. Curry, R.L. Martuza, D.N. Louis, O. Rozenblatt-Rosen, M.L. Suvà, A. Regev, B.E. Bernstein, in: Single-cell RNA-seq Highlights Intratumoral Heterogeneity in Primary Glioblastoma 344, 2014, pp. 1396–1401.
[50] A. Saadatpour, G. Guo, S.H. Orkin, G.-C. Yuan, Characterizing heterogeneity in leukemic cells using single-cell gene expression analysis, Genome Biol. 15 (2014) 525.
[51] S. Ding, X. Chen, K. Shen, in: Single-cell RNA sequencing in breast cancer: Understanding tumor heterogeneity and paving roads to individualized therapy 40, 2020, pp. 329–344.
[52] L.G. Martelotto, T. Baslan, J. Kendall, F.C. Geyer, K.A. Burke, L. Spraggon, S. Piscuoglio, K. Chadalavada, G. Nanjangud, C.K.Y. Ng, P. Moody, S. D'Italia, L. Rodgers, H. Cox, A. da Cruz Paula, A. Stepansky, M. Schizas, H.Y. Wen, T. A. King, L. Norton, B. Weigelt, J.B. Hicks, J.S. Reis-Filho, Whole-genome single-cell copy number profiling from formalin-fixed paraffin-embedded samples, Nat. Med. 23 (2017) 376–385.
[53] A.K. Casasent, A. Schalck, R. Gao, E. Sei, A. Long, W. Pangburn, T. Casasent, F. Meric-Bernstam, M.E. Edgerton, N.E. Navin, Multiclonal invasion in breast tumors identified by topographic single cell sequencing, Cell 172 (2018) 205–217, e212.
[54] P. Dumas, G.D. Sockalingum, J. Sulé-Suso, Adding synchrotron radiation to infrared microspectroscopy: what's new in biomedical applications? Trends Biotechnol. 25 (2007) 40–44.
[55] N. Elmadany, E. Khalil, L. Vaccari, G. Birarda, I. Yousef, R. Abu-Dahab, Antiproliferative activity of the combination of doxorubicin/quercetin on MCF7 breast cancer cell line: a combined study using colorimetric assay and synchrotron infrared microspectroscopy, Infrared Phys. Technol. 95 (2018) 141–147.
[56] I.I. Patel, D.A. Shearer, S.W. Fogarty, N.J. Fullwood, L. Quaroni, F.L. Martin, J. Weisz, Infrared microspectroscopy identifies biomolecular changes associated with chronic oxidative stress in mammary epithelium and stroma of breast tissues from healthy young women, Cancer Biol. Ther. 15 (2014) 225–235.
[57] H.T. Mohamed, V. Untereiner, G. Cinque, S.A. Ibrahim, M. Götte, N.Q. Nguyen, R. Rivet, G.D. Sockalingum, S. Brézillon, in: Infrared Microspectroscopy and Imaging Analysis of Inflammatory and Non-inflammatory Breast Cancer Cells and Their GAG Secretome 25, 2020, p. 4300.
[58] A.L.M. Batista de Carvalho, A.P. Mamede, A. Dopplapudi, V. Garcia Sakai, J. Doherty, M. Frogley, G. Cinque, P. Gardner, D. Gianolio, L.A.E. Batista de Carvalho, M.P.M. Marques, Anticancer drug impact on DNA – a study by neutron spectroscopy coupled with synchrotron-based FTIR and EXAFS, Phys. Chem. Chem. Phys. 21 (2019) 4162–4175.
[59] H.T. Mohamed, M. El-Shinawi, M.A. Nouh, A.R. Bashtar, E.T. Elsayed, R. J. Schneider, M.M. Mohamed, Inflammatory breast cancer: high incidence of detection of mixed human cytomegalovirus genotypes associated with disease pathogenesis, Front. Oncol. 4 (2014) 246.
[60] I. Shabo, J. Svanvik, Expression of macrophage antigens by tumor cells, Adv. Exp. Med. Biol. 714 (2011) 141–150.
[61] P. Allavena, A. Sica, G. Solinas, C. Porta, A. Mantovani, The inflammatory micro-environment in tumor progression: the role of tumor-associated macrophages, Crit. Rev. Oncol. Hematol. 66 (2008) 1–9.
[62] J.M. Pawelek, Cancer-cell fusion with migratory bone-marrow-derived cells as an explanation for metastasis: new therapeutic paradigms, Future Oncol. 4 (2008) 449–452.
[63] J.M. Pawelek, Tumour-cell fusion as a source of myeloid traits in cancer, Lancet Oncol. 6 (2005) 988–993.
[64] J.M. Pawelek, A.K. Chakraborty, Fusion of tumour cells with bone marrow-derived cells: a unifying explanation for metastasis, Nat. Rev. Cancer 8 (2008) 377–386.
[65] B. Benner, L. Scarberry, L.P. Suarez-Kelly, M.C. Duggan, A.R. Campbell, E. Smith, G. Lapurga, K. Jiang, J.P. Butchar, S. Tridandapani, J.H. Howard, R.A. Baiocchi, T. A. Mace, W.E. Carson 3rd, Generation of monocyte-derived tumor-associated macrophages using tumor-conditioned media provides a novel method to study tumor-associated macrophages in vitro, J. Immunother. Cancer 7 (2019) 140.
[66] S.K. Biswas, A. Mantovani, Macrophage plasticity and interaction with lymphocyte subsets: cancer as a paradigm, Nat. Immunol. 11 (2010) 889–896.
[67] B.Z. Qian, J.W. Pollard, Macrophage diversity enhances tumor progression and metastasis, Cell 141 (2010) 39–51.